

Probing Three-Dimensional Magnetic Fields: I - Polarized Dust Emission

Yue Hu^{1,2}★, A. Lazarian^{2,3}†

¹*Department of Physics, University of Wisconsin-Madison, Madison, WI, 53706, USA*

²*Department of Astronomy, University of Wisconsin-Madison, Madison, WI, 53706, USA*

³*Centro de Investigación en Astronomía, Universidad Bernardo O'Higgins, Santiago, General Gana 1760, 8370993, Chile*

Accepted XXX. Received YYY; in original form ZZZ

ABSTRACT

The plane-of-the-sky component of interstellar magnetic fields can be traced in two dimensions using polarized dust emission. Its potential to access three-dimensional magnetic fields, including the inclination of the magnetic fields relative to the line-of-sight, is crucial for a variety of astrophysical problems. Based on the statistical features of the polarization fraction and the averaged POS Alfvén Mach number $\overline{M}_{A,\perp}$, we present a new method for estimating the inclination angle. The magnetic field fluctuations raised by MHD turbulence are taken into account in our method. By using synthetic dust emission from 3D MHD turbulence simulation, we show that the fluctuations are preferentially perpendicular to the mean magnetic field and magnify the depolarization effect. We analytically and numerically derive that the polarization fraction is characterized by both the inclination angle and magnetic field fluctuations. We propose and demonstrate that the mean inclination angle over a region of interest can be calculated from the polarization fraction in a strongly magnetized reference position, where $\overline{M}_{A,\perp}^2 \ll 1$. We test the new method in sub-Alfvénic, trans-Alfvénic, and moderately super-Alfvénic situations ($0.4 \lesssim M_A \lesssim 1.2$) and show that it recovers the mean inclination angle well. This method is extended to determine the inclination angle distribution over the sub-regions of a cloud.

Key words: ISM: general—ISM: structure—ISM: magnetic field—ISM: dust, extinction—turbulence

1 INTRODUCTION

In the interstellar medium (ISM), the magnetic field is one of the most important components (Planck Collaboration et al. 2016a,b; Han 2017; Clark & Hensley 2019; Hu et al. 2020a, 2022). It is important for balancing the ISM with gravity (Wurster & Li 2018; Abbate et al. 2020), regulating turbulent gas flows (Roche et al. 2018; Busquet 2020), and constraining cosmic ray's transport (Yan & Lazarian 2002, 2004; Xu & Yan 2013; Xu & Lazarian 2020; Hu et al. 2021a). In particular, magnetic field is a key factor influencing the dynamics of the star-forming process in molecular clouds (Mac Low & Klessen 2004; McKee & Ostriker 2007; Lazarian et al. 2012; Federrath & Klessen 2012; Hu et al. 2021c). In view of its importance, a number of ways to accessing the magnetic field have been proposed. Polarized dust (Lazarian 2007; Andersson et al. 2015; Planck Collaboration et al. 2015a, 2020; Fissel et al. 2016; Li et al. 2021) and synchrotron emissions (Xiao et al. 2008; Planck Collaboration et al. 2016c; Guan et al. 2021) trace the POS magnetic field, while Zeeman splitting (Crutcher 2004, 2012) and Faraday rotation (Haverkorn 2007; Taylor et al. 2009; Oppermann et al. 2012; Xu & Zhang 2016) measure reveal the LOS magnetic field strength. However, probing a three-dimensional magnetic field that includes both the POS and the line-of-sight (LOS) components at the same time remains a challenge.

Intense attempts have been undertaken to get the three-dimensional

magnetic field. For instance, Lazarian & Yuen (2018b) proposed a solution using the wavelength derivative of synchrotron polarization. Tahani et al. (2019, 2022) used the changed sign of Faraday rotation measurements to infer a toroidal, helical, and bow-shaped magnetic field morphology across the Orion-A and Perseus molecular clouds. Zhang et al. (2020) achieved a three-dimensional magnetic field via the fraction and direction of atomic gas's polarization. Thereafter, Hu et al. (2021b) suggested using MHD turbulence's anisotropic property inherited by young stellar objects to obtain a three-dimensional view of the magnetic field. Similarly, based on anisotropic MHD turbulence, Hu et al. (2021d) further extend the method to be applicable for Doppler-shifted emission lines in three-dimension. For the latter two methods, the LOS and POS components of the magnetic field's orientation and strength can be calculated simultaneously.

In addition to above mentioned approaches, an important step of probing the three-dimensional magnetic field via polarized dust emission was initiated by Chen et al. (2019). The POS magnetic field can be easily inferred from polarization direction based on the fact that dust grains preferentially align with their ambient magnetic fields (Lazarian & Hoang 2007; Lazarian 2007; Andersson et al. 2015)). To achieve a three-dimensional picture, the inclination angle of the magnetic field relative to the LOS is crucial. As the inclination angle is one of the major agents of depolarizing thermal emission from dust, the polarization fraction intrinsically inherits the angle's information. Therefore, Chen et al. (2019) estimated the inclination angle based on the statistical properties of the observed polarization fraction. Their method assumes an ideal scenario that there is no

★ E-mail: yue.hu@wisc.edu

† E-mail: alazarian@facstaff.wisc.edu

fluctuation in neither magnetic field's POS or LOS components. This assumption holds only for strongly magnetized mediums. However, molecular clouds are typically trans-Alfvénic or even super-Alfvénic (Federrath et al. 2016; Hu et al. 2019; Hwang et al. 2021; Li et al. 2021), in which the fluctuation is not negligible.

In the paper below, we propose a simple configuration of magnetic fields along the LOS considering the existence of a global mean magnetic field and its fluctuations. This configuration is based on the advanced understanding of MHD turbulence, i.e., the most significant fluctuations preferentially appear in the direction perpendicular to the mean field (Goldreich & Sridhar 1995; Lazarian & Vishniac 1999; Cho & Lazarian 2003). By incorporating the magnetic field fluctuations, this work aims at developing a technique to probe the three-dimensional magnetic field in sub-, trans- and super-Alfvénic mediums. In addition to the observed polarization fraction, our technique requires the knowledge of the POS Alfvén Mach number's distribution. We test this method via the synthetic dust emission generated by 3D MHD turbulence simulations.

This paper is organized as follows. We briefly review the basic concepts of MHD and show the derivation of estimating the magnetic field inclination angle from the Stokes parameters of polarized dust emission. In § 3, we give the details of the simulation's setup and numerical method. We applied our method to the simulations in § 4 and make a comparison with the method proposed in Chen et al. (2019). In § 5, we discuss several approaches of getting the POS Alfvén Mach number's distribution. We summarize our results in § 6.

2 THEORETICAL CONSIDERATION

2.1 Essential of MHD turbulence

Our understanding of MHD turbulence has been significantly changed in the past decades. MHD turbulence was initially considered to be isotropic despite the existence of magnetic fields (Iroshnikov 1963; Kraichnan 1965). However, a number of numerical studies (Montgomery & Turner 1981; Shebalin et al. 1983; Higdon 1984; Kraichnan 1965; Montgomery & Matthaeus 1995; Maron & Goldreich 2001; Kowal & Lazarian 2010; Hu et al. 2021d) and in situ measurements of solar wind (Wang et al. 2016) revealed that the turbulence is anisotropic rather than isotropic when magnetic field's role is not negligible.

A cornerstone of the anisotropic and incompressible MHD turbulence theory was given by Goldreich & Sridhar (1995), denoted as GS95. The key to understanding the anisotropy of MHD turbulence is that velocity and magnetic field fluctuations are smaller than the local mean magnetic field. This makes the local mean-field instead of fluctuations dominate the dynamics. Along the local mean field, the Alfvén wave is propagating with a dispersion relation of $\omega = k_{\parallel} v_A$, where k_{\parallel} is a wavevector parallel to the mean magnetic field and v_A is Alfvén speed. Besides, in the case of weak interaction mean-field, turbulence creates a “perpendicular cascade,” with the perpendicular wavenumber k_{\perp} increasing while k_{\parallel} stays constant. This cascade enhances the nonlinearity, described by $\zeta = \sigma v_{\perp} k_{\perp} / v_A k_{\parallel}$, which is the ratio of the mean-field term to the nonlinear term. When turbulence becomes marginally strong, $\zeta \approx 1$, the nonlinear cascading time become close to the dynamical wave-period $\tau_{\text{casc}} \sim \tau_{\text{dyn}}$. In this situation, a “critical balance” of $\zeta \approx 1$ is statistically maintained in the further marginally cascade and the cascading follows the Kolmogorov scaling $v_{\perp} \propto k_{\perp}^{-1/3}$. Consequently, a highly anisotropic

ratio appears:

$$\frac{k_{\perp}}{k_{\parallel}} \propto k_{\perp}^{1/3} \quad (1)$$

which indicates the ratio of perpendicular scale and parallel scale increases at small scales.

However, the derivation of GS95 is worked in Fourier space using the global reference frame defined by a global mean magnetic field. In this frame, the contribution from the largest scale gets dominated so that one cannot observe a scale-dependent anisotropy (Cho & Vishniac 2000).

The subsequent study of turbulent reconnection in Lazarian & Vishniac (1999) derived the anisotropy in a local reference frame, which is defined by the local mean magnetic field. They demonstrated that turbulent reconnection of the magnetic field is an intrinsic part of the MHD turbulent cascade. The reconnection enables the mixing of magnetic field lines perpendicular to the magnetic field direction. The mixing motions give minimal resistance to the motions of eddies perpendicular to the magnetic field lines. Consequently, the turbulence cascade is channeled to the perpendicular creating perpendicular fluctuations and velocity fluctuations get maximum along this direction.

From the induction equation, one can easily find that the magnetic field fluctuation at scale l is also perpendicular to the plane spanned by the global mean magnetic field $\langle \mathbf{B} \rangle$ and displacement vector $\hat{\xi}$ of plasma in an Alfvén turbulence (Cho & Lazarian 2003):

$$\delta \mathbf{B}_{l,\perp} = \frac{v_{l,\perp}}{v_A} (\langle \mathbf{B} \rangle \times \hat{\xi}), \quad (2)$$

where $v_{l,\perp}$ is velocity fluctuation perpendicular to local magnetic field at scale l and v_A is the Alfvén speed.

The above consideration is valid for incompressible Alfvén turbulence. In a real scenario, compressible turbulence in ISM consists of also fast and slow modes. Slow mode in high- β (β is the compressibility) plasma is similar to the pseudo-Alfvén mode in the incompressible regime, while at low- β it is density perturbations propagating with sonic speed parallel to magnetic field (Cho & Lazarian 2003; Lazarian & Pogosyan 2012). Both slow and fast modes in low- β plasma are highly anisotropic (Kandel et al. 2017). It suggests that in low- β molecular clouds, anisotropic modes dominate compressible turbulence and the magnetic field fluctuation is perpendicular to the field. Nevertheless, the fast mode in high- β turbulence is a purely compressible mode with an isotropic power spectrum. Although the maximum energy fraction of fast mode is only $\sim 20\%$ (Hu et al. 2021a), an additional consideration is probably necessary to deal with the isotropic fast mode in high- β MHD turbulence.

2.2 Estimating inclination angle from dust polarization

Based the fact that magnetic field fluctuation is preferentially perpendicular to the mean field, we start investigating the properties of polarized dust emission. We adopt dust polarization equations from Planck Collaboration et al. (2015b):

$$\begin{aligned} I(x, y) &= \int n [1 - p_0 (\sin^2 \gamma - 2/3)] dz, \\ Q(x, y) &= \int p_0 n \frac{B_x^2 - B_y^2}{B^2} dz, \\ U(x, y) &= \int p_0 n \frac{2B_x B_y}{B^2} dz, \\ \psi(x, y) &= \frac{1}{2} \tan^{-1} \left(\frac{U}{Q} \right), \end{aligned} \quad (3)$$

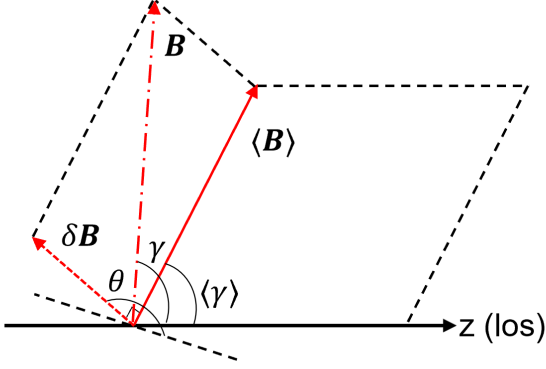


Figure 1. Illustration of the magnetic field configuration. $\langle \gamma \rangle$ is the mean inclination angle of the mean magnetic field $\langle \mathbf{B} \rangle$ with respect to the LOS. The mean field is changed by a perpendicular fluctuation $\delta \mathbf{B}$ which has an angle θ with respect to the plane defined by $\langle \mathbf{B} \rangle$ and the LOS. $\mathbf{B} = \langle \mathbf{B} \rangle + \delta \mathbf{B}$ is local total magnetic field.

where $n(x, y, z)$ is volume density, ϕ is polarization angle, and p_0 is a polarization fraction parameter related to the intrinsic polarization fraction (observationally measured value ~ 0.1). $B(x, y, z)$ denotes total magnetic field strength, while $B_x(x, y, z)$ and $B_y(x, y, z)$ are its x-axis component and y-axis component. Accordingly, the polarization fraction is:

$$p = \frac{\sqrt{Q^2 + U^2}}{I} = p_0 \frac{\sqrt{(\int n \frac{B_x^2 - B_y^2}{B^2} dz)^2 + (\int n \frac{2B_x B_y}{B^2} dz)^2}}{\int n dz - p_0 \int n (\sin^2 \gamma - 2/3) dz}, \quad (4)$$

We use a simple configuration of magnetic field. Assuming the local total magnetic field is the superposition of a mean magnetic field $\langle \mathbf{B} \rangle$ and a fluctuation $\delta \mathbf{B}(x, y, z)$:

$$\mathbf{B}(x, y, z) = \langle \mathbf{B} \rangle + \delta \mathbf{B}(x, y, z), \quad (5)$$

The mean-field also has a mean inclination angle $\langle \gamma \rangle$ and POS magnetic field angle $\langle \psi \rangle$. Owing to the properties of MHD turbulence, we consider the dominance of Alfvén and slow mode, for which the magnetic field fluctuation $\delta \mathbf{B}$ is perpendicular to the mean field. As the fluctuation $\delta \mathbf{B} \propto \mathbf{k} \times \langle \mathbf{B} \rangle$, where \mathbf{k} is wavevector, may not lie on the plane defined by $\langle \mathbf{B} \rangle$ and the LOS (i.e., the z-axis), we denote the angle between $\delta \mathbf{B}$ and the plane as θ (see Fig. 1). Accordingly, we incorporate the fluctuation into the x and y components:

$$\begin{aligned} B_x &= \langle B \rangle \sin \langle \gamma \rangle \cos \langle \psi \rangle + (\delta B \cos \theta) \cos \langle \gamma \rangle \cos \langle \psi \rangle + (\delta B \sin \theta) \sin \langle \psi \rangle, \\ B_y &= \langle B \rangle \sin \langle \gamma \rangle \sin \langle \psi \rangle + (\delta B \cos \theta) \cos \langle \gamma \rangle \sin \langle \psi \rangle - (\delta B \sin \theta) \cos \langle \psi \rangle, \end{aligned} \quad (6)$$

The fluctuations $\delta \gamma$ and $\delta \psi$ of $\langle \gamma \rangle$ and $\langle \psi \rangle$, respectively, are therefore introduced by $\delta \mathbf{B}$.

Note that the direction of $\delta \mathbf{B}$ is defined by the displacement vector and mean field. As the displacement vector varies in different spatial positions, we assume there is no preferential direction of $\delta \mathbf{B}$, then we

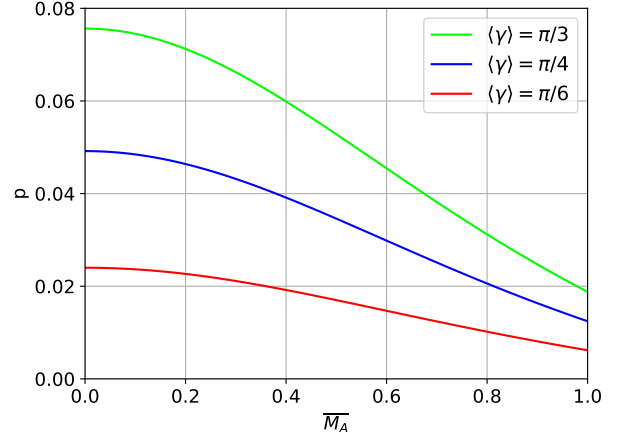


Figure 2. Analytical relation Eq. 8 of the polarization fraction p and $\overline{M_A}$.

integrate θ from 0 to 2π and take average value:

$$\begin{aligned} Q &= \frac{1}{2\pi} \int p_0 n \int_0^{2\pi} \frac{B_x^2 - B_y^2}{B^2} d\theta dz \\ &= \int p_0 n \frac{\cos(2\langle \psi \rangle) [\sin^2 \langle \gamma \rangle + \frac{1}{2} M_A^2 \cos^2 \langle \gamma \rangle - \frac{1}{2} M_A^2]}{1 + M_A^2} dz, \\ U &= \frac{1}{2\pi} \int p_0 n \int_0^{2\pi} \frac{2B_x B_y}{B^2} d\theta dz \\ &= \int p_0 n \frac{\sin(2\langle \psi \rangle) [\sin^2 \langle \gamma \rangle + \frac{1}{2} M_A^2 \cos^2 \langle \gamma \rangle - \frac{1}{2} M_A^2]}{1 + M_A^2} dz, \\ \frac{1}{2\pi} \int_0^{2\pi} \sin^2 \gamma d\theta &= \frac{1}{2\pi} \int_0^{2\pi} (1 - \cos^2 \gamma) d\theta \\ &= 1 - \frac{M_A^2 \sin^2 \langle \gamma \rangle}{2(M_A^2 + 1)} - \frac{\cos^2 \langle \gamma \rangle}{M_A^2 + 1}, \end{aligned} \quad (7)$$

Here $M_A = \delta B / \langle B \rangle$ is local Alfvén Mach number. Combining Eqs. 6 and 7, the polarization fraction can be written as:

$$p = \frac{p_0}{1 + \overline{M_A}^2} \cdot \frac{\sin^2 \langle \gamma \rangle (1 - \frac{1}{2} \overline{M_A}^2)}{1 - p_0 (1/3 - \frac{\sin^2 \langle \gamma \rangle (\overline{M_A}^2 - 2) + 2}{2(\overline{M_A}^2 + 1)})}, \quad (8)$$

Here we simplify the equation by the mean value $\overline{M_A}$ average along the LOS. Note upper "-" symbol means LOS average, while $\langle \dots \rangle$ is averaged over the volume of interests. In particular, as shown in Fig. 2, the fluctuation amplifies the depolarization effect so that p get its minimum value at large $\overline{M_A}$. Therefore, in the situation that the fluctuation vanishes, the value of p is.

$$\begin{aligned} p &= \frac{p_0 \sin^2 \langle \gamma \rangle}{1 - p_0 (\sin^2 \langle \gamma \rangle - \frac{2}{3})}, \quad \overline{M_A} \ll 1, \\ \sin^2 \langle \gamma \rangle &= \frac{p(1 + \frac{2}{3} p_0)}{p_0(1 + p)}, \quad \overline{M_A} \ll 1. \end{aligned} \quad (9)$$

In observation, $\sin^2 \langle \gamma \rangle$ can be calculated when p_0 is available. Chen et al. (2019) showed that within gas structures of different scales, such as molecular clouds, clumps, and dense cores, p_0 can be recovered

Model	M_s	M_A	Resolution	β
A0	5.38	0.41	792^3	0.01
A1	5.40	0.61	792^3	0.03
A2	5.23	0.95	792^3	0.07
A3	5.12	1.13	792^3	0.10

Table 1. Description of MHD simulations. The compressibility of turbulence is characterized by $\beta = 2(\frac{M_A}{M_s})^2$.

approximately from the maximum polarization fraction p_{\max} by:

$$p_0 = \frac{3p_{\max}}{3 + p_{\max}}. \quad (10)$$

Such information can potentially provide a powerful probe of the dust grain properties among various physical scales and at different evolutionary stages during star formation. Compared with Eq. 9, this expression implicitly correspondence to the case that the inclination angle is 90° . By searching for a number of sampling positions, it is possible to find a place, in which the local inclination angle $\gamma = \langle \gamma \rangle + \delta\gamma \sim 90^\circ$, and get the value of p_{\max} . Here $\delta\gamma$ means the fluctuations of inclination angle. However, as we will discuss in the following, this constrains the range of M_A or $\langle \gamma \rangle$.

Suppose that we have p_0 available, we can calculate the distribution of total Mach number explicitly from the observed polarization fraction p :

$$\overline{M_{A,\perp}^2} = \frac{p_0 \sin^2 \langle \gamma \rangle (1 + p) - p(1 + \frac{2}{3}p_0)}{\frac{1}{2}p_0 \sin^2 \langle \gamma \rangle (1 + p) + p(1 - \frac{1}{3}p_0)}, \quad (11)$$

In the absence of fluctuations, Eq. 11 equals zero and [Chen et al. \(2019\)](#) generalized it to every LOS with the replacement of $\sin^2 \langle \gamma \rangle$ by $\sin^2 \bar{\gamma}_{\text{Ch}}$:

$$\sin^2 \bar{\gamma}_{\text{Ch}} = \frac{p(1 + \frac{2}{3}p_0)}{p_0(1 + p)}, \quad (12)$$

The subscript "Ch" emphasises that this expression is obtained in [Chen et al. \(2019\)](#) assuming no fluctuations of magnetic field. Note Eq. 11 implicitly should give a non negative value. As $pp_0 \ll 1$, the condition $p_0 \sin^2 \langle \gamma \rangle \geq p$ should be satisfied at least.

Moreover, the POS projected value $\overline{M_{A,\perp}}$ can be evaluated by several methods and we know that $\overline{M_{A,\perp}} \sin \bar{\gamma} = \overline{M_A}$. The distribution of $\bar{\gamma}$ can be obtained from Eq. 11:

$$\sin^2 \bar{\gamma} = \frac{1}{\overline{M_{A,\perp}^2}} \cdot \frac{p_0 \sin^2 \langle \gamma \rangle (1 + p) - p(1 + \frac{2}{3}p_0)}{\frac{1}{2}p_0 \sin^2 \langle \gamma \rangle (1 + p) + p(1 - \frac{1}{3}p_0)}. \quad (13)$$

However, the assumption of perpendicular fluctuations is a statistical concept of MHD turbulence so that it holds only for sufficient samples. For each individual LOS, the fluctuations are not necessarily perpendicular to the mean magnetic field. Therefore, an additional technical approach is required. Otherwise the generalization of Eq. 13 to each grid pixel might be inaccurate. We discuss the possibility of using Eq. 13 to get pixelized distributions of inclination angle in § 5.

Here we introduce how to get obtain the mean inclination angle instead of the pixelized local one. Eq. 8 can be expressed as:

$$p = \frac{p_0}{1 + \overline{M_{A,\perp}^2} \sin^2 \bar{\gamma}} \cdot \frac{\sin^2 \langle \gamma \rangle (1 - \frac{1}{2}\overline{M_{A,\perp}^2} \sin^2 \bar{\gamma})}{1 - p_0(1/3 - \frac{\sin^2 \langle \gamma \rangle (\overline{M_{A,\perp}^2} \sin^2 \bar{\gamma} - 2) + 2)}{2(\overline{M_{A,\perp}^2} \sin^2 \bar{\gamma} + 1)}}, \quad (14)$$

here $\bar{\gamma}$ is the inclination angle averaged along the LOS. In the situation

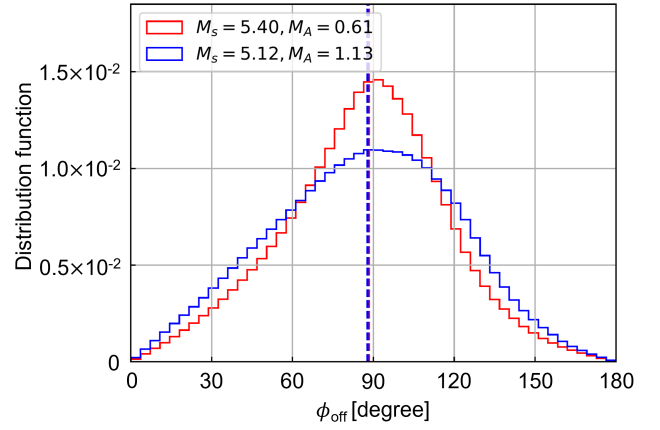


Figure 3. Histogram of the relative angle ϕ_{off} between the magnetic field fluctuation $\delta \mathbf{B}$ and mean magnetic field $\langle \mathbf{B} \rangle$. Dashed line indicates the median value.

of $\overline{M_{A,\perp}^2} \ll 1$, the contribution from $\overline{M_{A,\perp}^2} \sin^2 \bar{\gamma}$ is negligible. If one can find a POS position corresponding to minimum value of $\overline{M_{A,\perp}^2} \ll 1$, Eq. 14 reduces to:

$$p_{\text{off}} = \frac{p_0 \sin^2 \langle \gamma \rangle_{\text{off}}}{1 - p_0(\sin^2 \langle \gamma \rangle_{\text{off}} - \frac{2}{3})}, \quad \min\{\overline{M_{A,\perp}^2}\} \ll 1, \quad (15)$$

where p_{off} is the polarization fraction corresponding to the minimum $\overline{M_{A,\perp}^2}$. Equivalently, the mean inclination angle is:

$$\sin^2 \langle \gamma \rangle_{\text{off}} = \frac{p_{\text{off}}(1 + \frac{2}{3}p_0)}{p_0(1 + p_{\text{off}})}, \quad \min\{\overline{M_{A,\perp}^2}\} \ll 1, \quad (16)$$

The subscript "off" is used to distinguish from the mean inclination angle calculated by Eq. 9. In particular, Eq. 9 and Eq. 16 are different. Eq. 9 uses the local polarization fraction, while Eq. 16 requires the knowledge of polarization fraction and $\overline{M_{A,\perp}^2}$ at a reference position. In this work, we explore the combination of Eqs. 10 and 16 in obtaining three-dimensional magnetic field:

$$\sin^2 \langle \gamma \rangle_{\text{off}} = \frac{p_{\text{off}}(1 + p_{\max})}{p_{\max}(1 + p_{\text{off}})}, \quad \min\{\overline{M_{A,\perp}^2}\} \ll 1, \quad (17)$$

For simplicity, we calculate the distribution of $\overline{M_{A,\perp}^2}$ from numerical simulations directly. To implement it in observation, additional approaches of measuring $\overline{M_{A,\perp}^2}$ are required. We list several possible solutions in § 5.

2.3 Applicable regimes

The derivation of Eq. 16 is based on the anisotropic properties of MHD turbulence. As we discussed above, this consideration is valid in low- β molecular cloud while the treatment may be different when isotropic fast mode gets more significant in high- β MHD turbulence.

Eq. 10 is crucial to derive the inclination angle. [Chen et al. \(2019\)](#) argued that p_{\max} depends purely on the intrinsic properties of dust grain. However, as shown in Eq. 8, p_{\max} is also correlated with the inclination angle. To have an accurate estimation of p_0 , it requires to find a reference position, in which the local inclination angle (i.e., the mean angle plus the angle fluctuations) equals 90° . The corresponding local polarization fraction then can be used for Eq. 10.

This, however, constrains the either local M_A or $\langle \gamma \rangle$ in order to

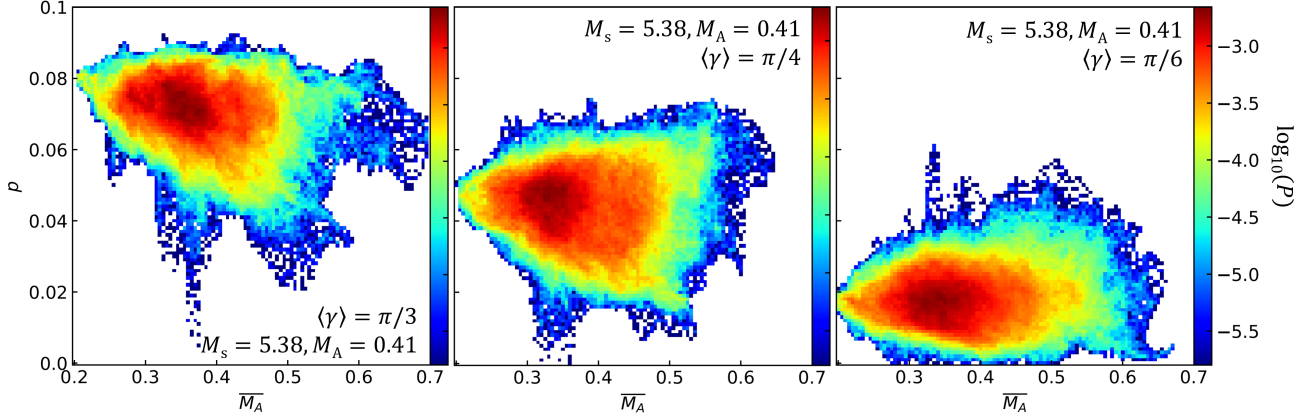


Figure 4. 2D histogram of polarization fraction p and projected total Alfvén Mach number $\overline{M_A}$ in the conditions of various mean inclination angle $\langle \gamma \rangle$. P denotes the percent of sampling points.

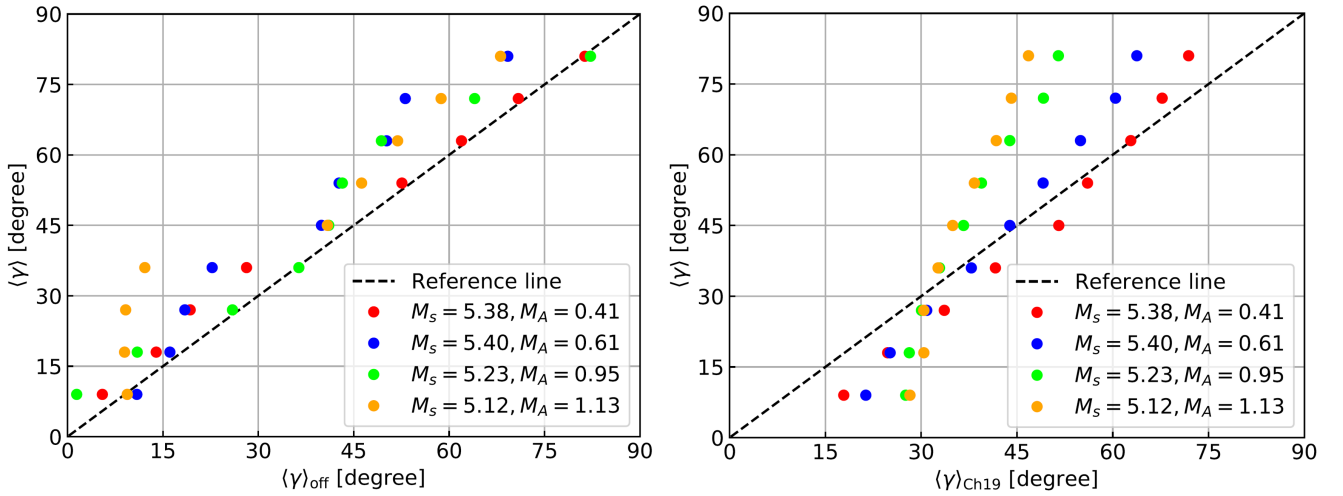


Figure 5. Comparison of the mean inclination angle $\langle \gamma \rangle_{\text{off}} / \langle \gamma \rangle_{\text{Ch19}}$ (left/right) with the real inclination angle $\langle \gamma \rangle$ of the simulation. $\langle \gamma \rangle_{\text{off}}$ is derived in this work, while $\langle \gamma \rangle_{\text{Ch19}}$ was proposed by [Chen et al.\(2019\)](#).

locally achieve $\gamma = \langle \gamma \rangle + \delta\gamma \sim 90^\circ$. For the simplest case that the $\delta\mathbf{B}$ lies on the plane defined by $\langle \mathbf{B} \rangle$ and the LOS (see Fig. 1), the local inclination angle is then $\gamma = \langle \gamma \rangle + \tan^{-1}(\delta B / \langle B \rangle) = \langle \gamma \rangle + \tan^{-1}(M_A)$. Within the assumption that magnetic field fluctuation is negligible (i.e., $M_A \sim 0$), the local inclination angle reaches 90° only when $\langle \gamma \rangle = 90^\circ$. Therefore, in order to find p_{max} by searching for a number of sampling positions, it requires variation of magnetic field at different positions. In the case of sub-Alfvénic medium with a small inclination angle, p_{max} can be underestimated.

2.4 Sub-region sampling

The combination of Eq. 16 and Eq. 10 could reveal the mean inclination angle for a given cloud. As the mean value of $\overline{M_{A,\perp}}$ is also available, the mean total Mach number can be easily accessed $\langle \overline{M_{A,\perp}} \rangle \sin \langle \gamma \rangle = \langle \overline{M_A} \rangle$.

The accuracy of this method depends on (i) presence of a mean magnetic field; (ii) $\min\{\overline{M_{A,\perp}}^2\} \ll 1$; (iii) the samples within a region

is sufficient so that the perpendicular fluctuations appear; and (iv) the value of p_{max} . Therefore, it is not necessary to choose the full cloud as the object for the application. Once the four conditions are satisfied for a sub-region within the cloud, one can access the three-dimensional magnetic field there. We denote this zoom-in procedure as sub-region sampling.

3 NUMERICAL METHOD

The numerical simulations used in this work are generated through ZEUS-MP/3D code ([Hayes et al. 2006](#)). In the Eulerian frame, we simulate an isothermal cloud by solving the ideal MHD equations with periodic boundary conditions. The cloud is initiated with uniform density field $\langle \rho \rangle$ and magnetic field $\langle \mathbf{B} \rangle$ along the x-axis, which is perpendicular to the LOS.

Considering pure turbulence cases without self-gravity. Kinetic energy is solenoidally injected at wavenumber ~ 2 to produce a Kolmogorov spectrum. The solenoidal driving mechanism can also

generate a compressive component. We continuously drive turbulence and dump the data until the turbulence gets fully developed at one sound crossing time. The simulation is grid into 792^3 cells and turbulence gets numerically dissipated at scales $\approx 10 - 20$ cells. Turbulence induces also fluctuations $\delta \mathbf{B}$ and $\delta \rho$ of magnetic field and density field, respectively.

Simulation of MHD turbulence is scale-free. Its properties are characterized by the sonic Mach number $M_s = v_{\text{inj}}/c_s$ and Alfvénic Mach number $M_A = v_{\text{inj}}/v_A = \delta B_{\text{inj}}/\langle B \rangle$, where δB_{inj} is magnetic field fluctuation at injection scale. The sound speed $c_s \approx 0.192$ in the code unit is fixed due to the isothermal equation of state. To simulate different ISM conditions, we change the initial uniform magnetic field, density field, and injected kinetic energy to achieve various M_A and M_s values. In this work, we refer to the simulations in Tab. 2.2 by their model name or key parameters. Similar simulations have been used in [Yuen & Lazarian \(2017a\)](#) and [Hu et al. \(2020b\)](#).

Synthetic dust emission is then calculated from Eq. 3 by extracting necessary information from MHD simulation. The 3D inclination angle γ_{3D} at each cell and mean inclination angle $\langle \gamma \rangle$ of the simulation are calculated from:

$$\gamma_{3D} = \cos^{-1} \left(\sqrt{\frac{B_z^2}{B_x^2 + B_y^2 + B_z^2}} \right), \quad (18)$$

$$\langle \gamma \rangle = \tan^{-1} \left(\frac{\langle \sin \gamma_{3D} \rangle}{\langle \cos \gamma_{3D} \rangle} \right),$$

Note here $\langle \dots \rangle$ means averaging over all cells. We rotate the simulation box to achieve different inclination angles.

In particular, M_A^{3D} at each cell and its POS projection $M_{A,\perp}$ are approximated by:

$$M_A^{3D} = (B - \langle B \rangle) / \langle B \rangle, \quad (19)$$

$$M_{A,\perp} = \frac{M_A^{3D}}{\sin \gamma_{3D}},$$

averaging $M_{A,\perp}$ along each LOS gives $\overline{M_{A,\perp}}$ at each cell accordingly.

We compare the global inclination angle estimated by our approach with the one proposed by [Chen et al. \(2019\)](#) (hereafter, Ch19). We note the mean inclination angle inferred from Eq. 16 as:

$$\langle \gamma \rangle_{\text{off}} = \sqrt{\sin^{-1} \left[\frac{p_{\text{off}}(1 + \frac{2}{3}p_0)}{p_0(1 + p_{\text{off}})} \right]}, \quad \min\{\overline{M_{A,\perp}}^2\} \ll 1, \quad (20)$$

and the one calculated from Ch19 as:

$$\langle \gamma \rangle_{\text{Ch19}} = \langle \sqrt{\sin^{-1} \left[\frac{p(1 + \frac{2}{3}p_0)}{p_0(1 + p)} \right]} \rangle, \quad (21)$$

here the average is performed in an angular statistic way.

The relative orientation between the measured inclination angle and real inclination angle of the simulation is measured with the Alignment Measure (AM; [González-Casanova & Lazarian 2017](#)), defined as:

$$\text{AM} = 2(\langle \cos^2 \theta_r \rangle - \frac{1}{2}) \quad (22)$$

where θ_r is the relative angle between the two angle. AM is a relative scale ranging from -1 to 1, with AM = 1 indicating that two angles being globally parallel, and AM = -1 denoting that the two are globally orthogonal.

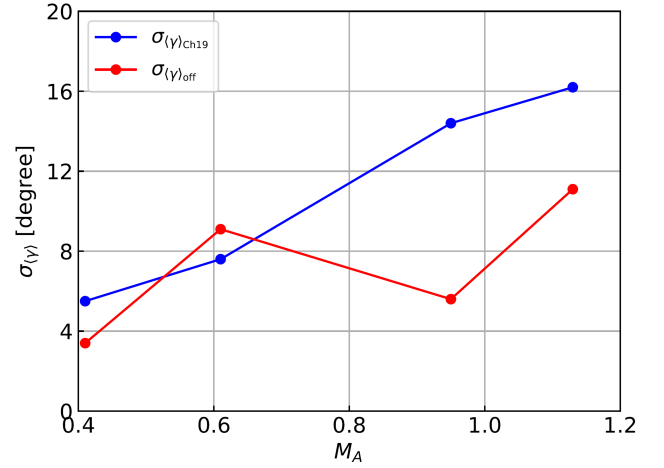


Figure 6. The averaged deviation of the estimated inclination angle and actual inclination angle. $\sigma_{\langle \gamma \rangle_{\text{off}}}$ represents the averaged absolute difference between $\langle \gamma \rangle_{\text{off}}$ and $\langle \gamma \rangle$, while $\sigma_{\langle \gamma \rangle_{\text{Ch19}}}$ is for $\langle \gamma \rangle_{\text{Ch19}}$ and $\langle \gamma \rangle$.

4 RESULTS

4.1 Global estimation of the inclination angle

Fig. 3 presents the histogram of the relative angle ϕ_{off} between the magnetic field fluctuation $\delta \mathbf{B}$ and mean magnetic field $\langle \mathbf{B} \rangle$. The histogram is close to a Gaussian distribution with a median value concentrated on 90° around. This value of $\phi_{\text{off}} \approx 90^\circ$ is crucial for in our theoretical assumption that MHD turbulence's anisotropy appears when sample is sufficient. Also, it suggest the dominance of Alfvén mode and slow mode.

Fig. 4 shows the 2D histograms of polarization fraction p and projected total Alfvén Mach number $\overline{M_A}$. We also vary the mean inclination angle $\langle \gamma \rangle$. In general, p tends to be reduced at large $\overline{M_A}$ range, which indicates a strong magnetic field fluctuation. The value of $\langle \gamma \rangle$ strongly affects maximum and average value of p . p is highly depolarized in small inclination angle cases and the maximum p usually appears with large $\overline{M_A}$. The value of p_{max} in sub-Alfvénic case (small $\overline{M_A}$), therefore, introduces uncertainty to the estimation of $\langle \gamma \rangle_{\text{off}}$ (see § 2). For instance, when the real $\langle \gamma \rangle$ equals $\pi/6$, we see $p_{\text{max}} \sim 0.06$ and $p_{\text{off}} \sim 0.02$. $p_{\text{max}} \sim 0.06$, however, does not correspond to the local inclination angle $\sim 90^\circ$, since we observe a higher value $p_{\text{max}} \sim 0.09$ when the real $\langle \gamma \rangle$ equals $\pi/3$. Accordingly to Eq. 16, $p_{\text{max}} \sim 0.06$ gives $\langle \gamma \rangle_{\text{off}} \sim 36^\circ = \pi/5$, while $p_{\text{max}} \sim 0.09$ results in $\langle \gamma \rangle_{\text{off}} \sim 30^\circ = \pi/6$. The smaller p_{max} raises a uncertainty of 6° .

A comparison with the global $\langle \gamma \rangle$ of full simulation cube obtained via Ch19's method is presented in Fig. 5. For $\langle \gamma \rangle$ calculated through our method (denoted as $\langle \gamma \rangle_{\text{off}}$), generally it is well compatible with the actual inclination angle of the simulation, although $\langle \gamma \rangle_{\text{off}}$ gives slightly underestimated values. This underestimation might come from two reasons: (i) the approximation of p_0 using Eq. 9; (ii) The fluctuation of p_{off} , which is crucial for our calculation. There are a number of p_{off} values for which their corresponding $\overline{M_{A,\perp}}$ is much less than one. Therefore, p_{off} 's value can introduce uncertainty. As for Ch19's method, its estimation agrees with actual angles better in strong magnetic field cases, i.e., sub-Alfvénic $M_A = 0.41$ and 0.61 . The overestimation in the small inclination angle case is raised by the underestimation of p_{max} . However, the estimated angle diverges at weak magnetic field conditions, i.e., trans- and super-Alfvénic $M_A =$

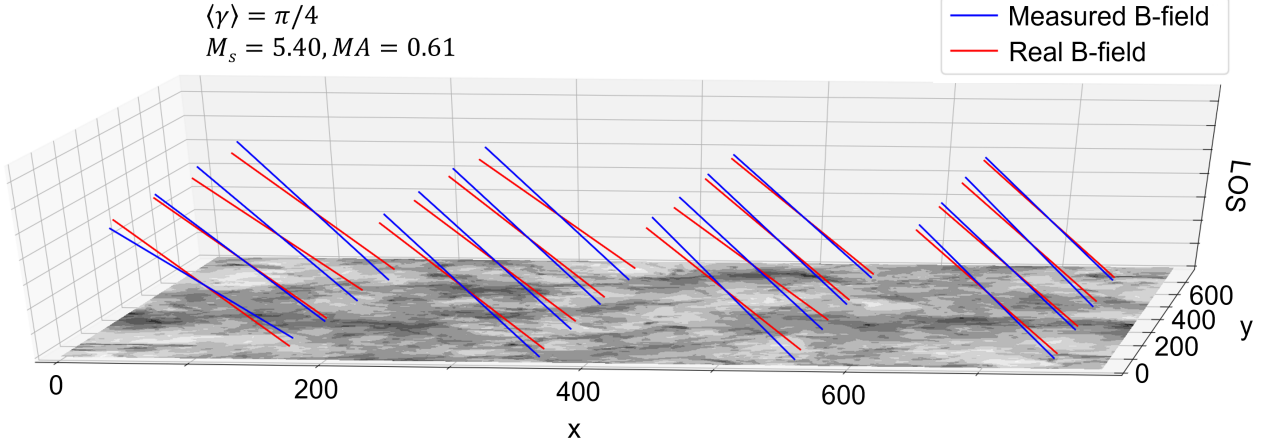


Figure 7. An example of the inclination angles measured for sixteen sub-regions, whose size is $198 \times 198 \text{ cell}^2$. Each magnetic field vector is constructed by the POS magnetic field’s position angle (i.e., $\psi + \pi/2$) inferred from Stokes parameters and the inclination angle of either measured $\langle \gamma \rangle_{\text{off}}$ (blue) or actual $\langle \gamma \rangle$ (red). Note that the magnetic field is averaged along the LOS. The third axis of LOS is for 3D visualization purpose having no distance information here. The total intensity map I is placed on the POS, i.e., the xy plane.

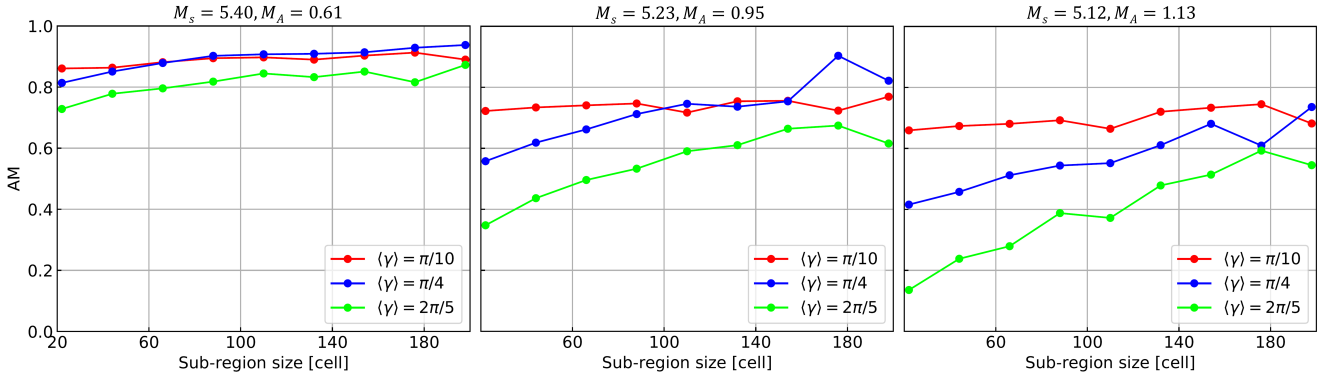


Figure 8. The AM of $\langle \gamma \rangle_{\text{off}}$ and $\langle \gamma \rangle_{\text{sub}}$ as a function of the sub-region’s size. $\langle \gamma \rangle$ denotes the global mean inclination angle of the full simulation box.

0.95 and 1.13. This is caused by significant fluctuations of weak magnetization, which breaks Ch19’s assumption that the fluctuations are negligible.

Fig. 6 shows the averaged deviation of the estimated inclination angle and actual angle. We calculate the absolute difference between $\langle \gamma \rangle_{\text{off}}$ (or $\langle \gamma \rangle_{\text{Ch19}}$) and $\langle \gamma \rangle$. The calculation is performed for all data points shown in Fig. 5 and takes their average. The deviation of $\sigma_{\langle \gamma \rangle_{\text{Ch19}}}$ monotonically increases when M_A gets larger. It increases from $\approx 5^\circ$ ($M_A = 0.41$) to $\approx 16^\circ$ ($M_A = 1.13$). The trend of the deviation $\sigma_{\langle \gamma \rangle_{\text{off}}}$ is more complex. In general, it has a similar value with $\sigma_{\langle \gamma \rangle_{\text{Ch19}}}$ in sub-Alfvénic case. In trans- and super-Alfvénic cases, despite that $\sigma_{\langle \gamma \rangle_{\text{off}}}$ slows increases, it is smaller than $\sigma_{\langle \gamma \rangle_{\text{Ch19}}}$. Unlike Ch19, $\langle \gamma \rangle_{\text{off}}$ ’s calculation depends on whether the minimum value of $\overline{M_{A,\perp}}$ is negligible. Due to the fluctuation of $\overline{M_{A,\perp}}$, even in trans- and super-Alfvénic conditions, its minimum values arrives sub-Alfvénic range so that its assumption holds on and the uncertainty is smaller.

4.2 Sub-region sampling

As discussed above, our method depends on two conditions: (i) the existence of a mean field; (ii) the minimum value of $\overline{M_{A,\perp}}^2$ is much smaller than 1. Thus, it is not necessary to perform the calculation to the full cloud or simulation. This method can be generalized to sub-regions satisfied with the conditions. In this section, we test the relation of $\langle \gamma \rangle_{\text{off}}$ ’s accuracy and the sub-region’s size.

Fig. 7 present an example of the inclination angles measured for sixteen sub-regions, whose size is $198 \times 198 \text{ cell}^2$. For simplicity, the sub-region is defined as a square and we refer to its size using length scale in the following. Each vector is constructed by the POS magnetic field’s position angle (i.e., $\psi + \pi/2$) inferred from Stokes parameters (see § 2) and the inclination angle of either measured $\langle \gamma \rangle_{\text{off}}$ or actual $\langle \gamma \rangle_{\text{sub}}$, which is the mean inclination angle of a sub-region. As we see, globally the simulation has inclination $\langle \gamma \rangle = \pi/4$ and the POS magnetic field is along x -axis. For each sub-region, while the magnetic field’s orientation exhibits slight variation, the measured inclination angles agree well with the actual angles.

Moreover, we test the accuracy of $\langle \gamma \rangle_{\text{off}}$ at various sub-region

sizes. The global agreement of $\langle \gamma \rangle_{\text{off}}$ and $\langle \gamma \rangle$ is quantified by the AM (see § 3). As shown in Fig. 8, in general AM increases for a large sub-region size. This can be easily understood as a large sub-region containing more sampling points so that the mean magnetic field is better defined compared with a small sub-region. A large sub-region size also mean the probability of finding out $\min\{\overline{M}_{A,\perp}^2\} \ll 1$ increases. Therefore, compared with the sub-Alfvénic case, the increment of AM at a large sub-region size is more significant in the super-Alfvénic case. Moreover, this also indicates that the accuracy of the estimated inclination angle mainly depends on the condition that $\min\{\overline{M}_{A,\perp}^2\} \ll 1$. The uncertainty raised by p_{max} is not significant.

In addition, we notice that a large global mean inclination angle $\langle \gamma \rangle$ is associated with a smaller AM value, in particular for small sub-region size. Intuitively this disagrees with our theoretical consideration that large $\langle \gamma \rangle$ suggests a small value of $\overline{M}_{A,\perp} = \overline{M}_A / \sin \overline{\gamma}$, which better constrains $\langle \gamma \rangle_{\text{off}}$. However, the crucial term in determining $\langle \gamma \rangle_{\text{off}}$ is $\overline{M}_{A,\perp}^2 \sin^2 \overline{\gamma}$ instead of $\overline{M}_{A,\perp}^2$ (see Eq. 14). The choice of using $\min\{\overline{M}_{A,\perp}^2\} \ll 1$ is based on the fact it is the only achievable variable in observation. For a given \overline{M}_A value, a small inclination angle significantly and non-linearly reduces the value of $\overline{M}_{A,\perp}^2 \sin^2 \overline{\gamma}$. For instance, $\sin^2(\pi/10)$ is smaller than $\sin^2(2\pi/5)$ in one order of magnitude. In this case, Eq. 16 is better constrained for a small inclination angle and, therefore, AM increases.

Fig. 9 presents the relation of $\min\{\overline{M}_{A,\perp}\}$ and AM (of $\langle \gamma \rangle_{\text{off}}$ and $\langle \gamma \rangle_{\text{sub}}$) calculated for each 22×22 cell² sub-region. The sub-region 22×22 cell² cells guarantees sufficient samples for characterizing overall statistical properties. First of all, as we expected, a small value of $\min\{\overline{M}_{A,\perp}\}$ is associated with large AM, i.e., high accuracy, as well large polarization fraction. For the case of $\langle \gamma \rangle = 2\pi/5$, AM drops to negative when $\min\{\overline{M}_{A,\perp}\} > 0.50$ at least. In this situation, the contribution from $\overline{M}_{A,\perp}^2 \sin^2 \overline{\gamma}$ is not negligible so that the assumption of Eq. 16 breaks. A smaller inclination angle $\langle \gamma \rangle = \pi/10$ shifts $\min\{\overline{M}_{A,\perp}\}$ to larger value and increases AM. For such a small $\langle \gamma \rangle$, $\min\{\overline{M}_{A,\perp}\}$ is less important in determine $\langle \gamma \rangle_{\text{off}}$. In observation, $\langle \gamma \rangle$ can be obtained from Eq. 16 targeting on the full cloud. Once the value of $\langle \gamma \rangle$ is available, the sub-region size can be selected accordingly. One should use a pretty large size when both $\min\{\overline{M}_{A,\perp}\} > 0.5$ and $\langle \gamma \rangle$ is large (for instance, $\langle \gamma \rangle > \pi/4$). Otherwise, if $\langle \gamma \rangle$ is small, the restriction on $\min\{\overline{M}_{A,\perp}\}$ and sub-region size can be released a bit.

5 DISCUSSION

5.1 Mapping the POS M_A distribution

In this work, we propose a new method of probing three-dimensional magnetic fields using the observed polarization fraction and measured $\overline{M}_{A,\perp}$ distribution. We list several approaches of getting $\overline{M}_{A,\perp}$ here.

The first way is using the polarization measurement. For instance, [Falceta-Gonçalves et al. \(2008\)](#) suggested a generalization of the Davis–Chandrasekhar–Fermi method ([Davis 1951](#); [Chandrasekhar & Fermi 1953](#)) to obtain the $\overline{M}_{A,\perp}$ by $\tan \delta\theta \sim \overline{M}_{A,\perp}$. Here $\delta\theta$ is the dispersion of the distribution of the polarization angles. Also, the $\overline{M}_{A,\perp}$ can also be calculated from the polarization fraction. The relation is proposed by [Lazarian et al. \(2018\)](#) that $\sigma_{\text{pol}\%} \sim \overline{M}_{A,\perp}^2$, where $\sigma_{\text{pol}\%}$ is the dispersion of polarization fraction. Although the measurement of the polarization angle's dispersion over a region reduces the observation's resolution, once the $\overline{M}_{A,\perp}$ distribution is

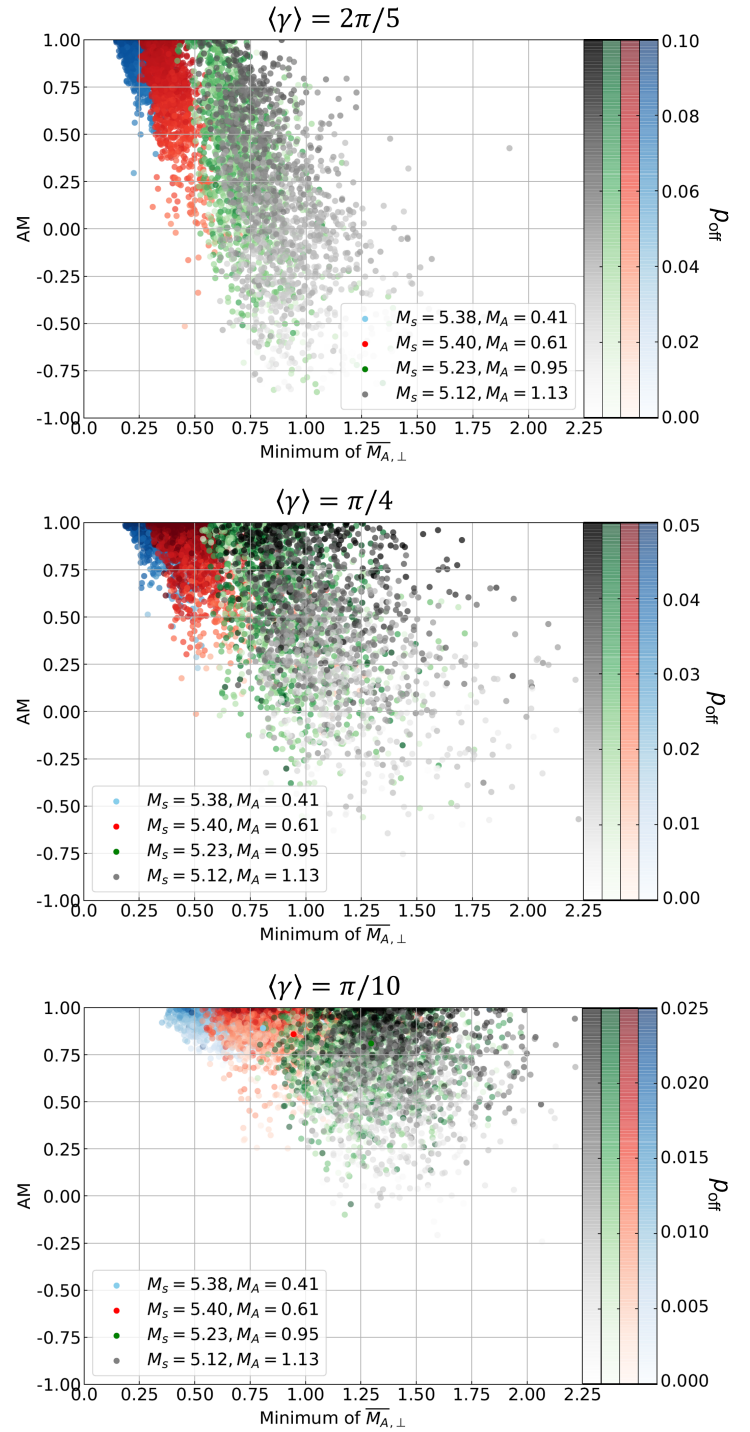


Figure 9. Scatter plots of $\min\{\overline{M}_{A,\perp}\}$ and AM (of $\langle \gamma \rangle_{\text{off}}$ and $\langle \gamma \rangle_{\text{sub}}$). $\min\{\overline{M}_{A,\perp}\}$ and AM are calculated for each 22×22 cell² sub-region. Color indicates the polarization fraction p_{off} corresponding to $\min\{\overline{M}_{A,\perp}\}$. $\langle \gamma \rangle$ denotes the global mean inclination angle of the full simulation box.

available, as presented in Lazarian et al. (2018), Hwang et al. (2021) and Li et al. (2021), one can access the three-dimensional magnetic field using our proposed technique.

The velocity gradient technique and the structure-function analysis are other ways of getting $\overline{M_{A,\perp}^2}$. The velocity gradient technique (VGT; González-Casanova & Lazarian 2017; Yuen & Lazarian 2017b; Lazarian & Yuen 2018a; Hu et al. 2018) is a novel method of tracing magnetic fields. It is rooted in MHD turbulence's anisotropy, i.e., the gradient of velocity fluctuation is perpendicular to the magnetic field. In addition to tracing the orientation, VGT is also capable of estimating the $\overline{M_{A,\perp}^2}$ distribution (Lazarian et al. 2018; Hu et al. 2019). The estimation uses the velocity gradient's dispersion, which is small in a strongly magnetized medium but is large for weak magnetization. By separating the cloud into a number of sub-regions, one can calculate the velocity gradient's dispersion and find the $\overline{M_{A,\perp}^2}$ distribution.

The structure-function analysis (SFA; Hu et al. 2021b; Xu & Hu 2021; Hu et al. 2021d) estimates $\overline{M_{A,\perp}^2}$ from the ratio of velocity fluctuations perpendicular and parallel to the POS magnetic field. Its foundation is also MHD turbulence's anisotropy, which suggests that the maximum amplitude of velocity fluctuation appears in the direction perpendicular to the magnetic field but the minimum value appears in the parallel direction. The ratio is positively proportional to $(\overline{M_{A,\perp}^2})^{-4/3}$.

Moreover, the VGT and SFA potentially contain the necessary information for getting pixelized distributions of total magnetic field strength and inclination angle from the Eq. 11. The dilemma of Eq. 11 is that we need sufficient samples to constrain turbulence's property, which does not appear in a single data point of dust polarization. However, using the basic foundation of VGT or SFA, the turbulence's property from Doppler-shifted lines usually has a higher resolution than polarization measurement. For example, the CO (1-0) emission line observed with the Green Bank telescope achieves a beam resolution $\sim 8''$. If one selects a sub-region size smaller than $80 \times 80 \text{ cell}^2$, the measured turbulence's property for each sub-region would have resolution $\sim 10'$, which is comparable with the Planck polarization measurement. This information, therefore, could be implemented in Planck polarization to obtain local magnetic field strength and inclination angle.

5.2 Comparison with Other Methods

Chen et al. (2019) proposed a method to calculate the inclination angle of the magnetic field. Assuming the magnetic field fluctuation is negligible along the LOS, their method calculates the inclination angle distribution using the local polarization fraction (see Eq. 12). However, the assumption holds only for the strongly sub-Alfvénic case, while molecular clouds are typically trans-Alfvénic or super-Alfvénic (Federrath et al. 2016; Hu et al. 2019; Hwang et al. 2021; Li et al. 2021). Even in the sub-Alfvénic case, the crucial value of p_{max} would be intrinsically underestimated and introduces uncertainty (see § 2).

In this work, we take into account the fluctuation of the magnetic field due to anisotropic MHD turbulence. We show that the local polarization fraction, in this case, depends on not only the inclination angle but also the magnetic field fluctuation. The fluctuation amplifies the depolarization effect. Consequently, the local polarization fraction does not accurately characterize the inclination angle using Eq. 12. We propose and demonstrate that only the polarization fraction in the reference position, in which $\overline{M_{A,\perp}^2} \ll 1$, is purely correlated with the mean inclination angle over a region of interest, since

the contribution from the fluctuation is insignificant there. The mean inclination angle thus can be calculated (see Eq. 16) once the distribution of $\overline{M_{A,\perp}^2}$ is available. In particular, our method is applicable to molecular clouds. Because trans-Alfvénic or super-Alfvénic clouds raise significant $\overline{M_{A,\perp}^2}$ fluctuations, one can easily find a position corresponding to $\overline{M_{A,\perp}^2} \ll 1$ by searching for sufficient samples.

Another two methods of tracing three-dimensional magnetic fields were proposed by Hu et al. (2021b) and Hu et al. (2021d). The two methods are based on MHD turbulence's anisotropic property, i.e., the maximum velocity fluctuation appears in the direction perpendicular to the magnetic field. Consequently, by measuring the three-dimensional velocity fluctuations of young stellar objects, which are accessible via the Gaia survey (Gaia Collaboration et al. 2016, 2018), one can find the three-dimensional magnetic fields (Hu et al. 2021b). Hu et al. (2021d), on the other hand, proposed to measure the velocity fluctuations using Doppler-shifted emission lines. It was shown that the ratio of maximum and minimum fluctuations within a given velocity channel is correlated with the velocity channel width, total Alfvén Mach number (M_A), and the inclination angle. Therefore, by varying the channel widths used for calculating the ratio, one can solve the M_A and inclination angle out simultaneously.

6 SUMMARY

Dust polarization is one of the most important ways to trace the magnetic fields in ISM. We propose a new technique to trace three-dimensional magnetic fields with the observed polarization fraction of polarized dust emission and the distribution of the POS Alfvén Mach number. Appealing to the MHD turbulence theory, we assume that the fluctuations are preferentially perpendicular to the mean magnetic field and amplify the depolarization effect. We analytically derive and numerically confirm that the polarization fraction corresponding to $\overline{M_{A,\perp}^2} \ll 1$ well characterizes the mean inclination angle. We test our technique using 3D MHD turbulence simulations and show that it is applicable to a wide range of physical conditions, including sub-Alfvénic, trans-Alfvénic, and moderately supers-Alfvénic mediums and that recovers the three-dimensional magnetic field direction quite well.

ACKNOWLEDGEMENTS

Y.H. and A.L. acknowledges the support of NASA ATP AAH7546. We acknowledge the allocation of computer time by the Center for High Throughput Computing (CHTC) at the University of Wisconsin-Madison.

DATA AVAILABILITY

The data underlying this article will be shared on reasonable request to the corresponding author.

REFERENCES

- Abbate F., Possenti A., Tiburzi C., Barr E., van Straten W., Ridolfi A., Freire P., 2020, *Nature Astronomy*, **4**, 704
- Andersson B. G., Lazarian A., Vaillancourt J. E., 2015, *ARA&A*, **53**, 501
- Busquet G., 2020, *Nature Astronomy*, **4**, 1126
- Chandrasekhar S., Fermi E., 1953, *ApJ*, **118**, 113

- Chen C.-Y., King P. K., Li Z.-Y., Fissel L. M., Mazzei R. R., 2019, *MNRAS*, **485**, 3499
- Cho J., Lazarian A., 2003, *MNRAS*, **345**, 325
- Cho J., Vishniac E. T., 2000, *ApJ*, **539**, 273
- Clark S. E., Hensley B. S., 2019, *ApJ*, **887**, 136
- Crutcher R. M., 2004, in Uyaniker B., Reich W., Wielebinski R., eds, The Magnetized Interstellar Medium. pp 123–132
- Crutcher R. M., 2012, *ARA&A*, **50**, 29
- Davis L., 1951, *Physical Review*, **81**, 890
- Falceta-Gonçalves D., Lazarian A., Kowal G., 2008, *ApJ*, **679**, 537
- Federrath C., Klessen R. S., 2012, *ApJ*, **761**, 156
- Federrath C., et al., 2016, *ApJ*, **832**, 143
- Fissel L. M., et al., 2016, *ApJ*, **824**, 134
- Gaia Collaboration et al., 2016, *A&A*, **595**, A1
- Gaia Collaboration et al., 2018, *A&A*, **616**, A1
- Goldreich P., Sridhar S., 1995, *ApJ*, **438**, 763
- González-Casanova D. F., Lazarian A., 2017, *ApJ*, **835**, 41
- Guan Y., et al., 2021, *ApJ*, **920**, 6
- Han J. L., 2017, *ARA&A*, **55**, 111
- Haverkorn M., 2007, in Haverkorn M., Goss W. M., eds, Astronomical Society of the Pacific Conference Series Vol. 365, SINS - Small Ionized and Neutral Structures in the Diffuse Interstellar Medium. p. 242 ([arXiv:astro-ph/0611090](https://arxiv.org/abs/astro-ph/0611090))
- Hayes J. C., Norman M. L., Fiedler R. A., Bordner J. O., Li P. S., Clark S. E., ud-Doula A., Mac Low M.-M., 2006, *ApJS*, **165**, 188
- Higdon J. C., 1984, *ApJ*, **285**, 109
- Hu Y., Yuen K. H., Lazarian A., 2018, *MNRAS*, **480**, 1333
- Hu Y., et al., 2019, *Nature Astronomy*, **3**, 776
- Hu Y., Yuen K. H., Lazarian A., 2020a, *ApJ*, **888**, 96
- Hu Y., Lazarian A., Bialy S., 2020b, *ApJ*, **905**, 129
- Hu Y., Lazarian A., Xu S., 2021a, arXiv e-prints, p. [arXiv:2111.15066](https://arxiv.org/abs/2111.15066)
- Hu Y., Xu S., Lazarian A., 2021b, *ApJ*, **911**, 37
- Hu Y., Lazarian A., Stanimirović S., 2021c, *ApJ*, **912**, 2
- Hu Y., Lazarian A., Xu S., 2021d, *ApJ*, **915**, 67
- Hu Y., Lazarian A., Wang Q. D., 2022, *MNRAS*, **511**, 829
- Hwang J., et al., 2021, *ApJ*, **913**, 85
- Iroshnikov P. S., 1963, *Azh*, **40**, 742
- Kandel D., Lazarian A., Pogossyan D., 2017, *MNRAS*, **464**, 3617
- Kowal G., Lazarian A., 2010, *ApJ*, **720**, 742
- Kraichnan R. H., 1965, *Physics of Fluids*, **8**, 1385
- Lazarian A., 2007, *J. Quant. Spectrosc. Radiative Transfer*, **106**, 225
- Lazarian A., Hoang T., 2007, *MNRAS*, **378**, 910
- Lazarian A., Pogossyan D., 2012, *ApJ*, **747**, 5
- Lazarian A., Vishniac E. T., 1999, *ApJ*, **517**, 700
- Lazarian A., Yuen K. H., 2018a, *ApJ*, **853**, 96
- Lazarian A., Yuen K. H., 2018b, *ApJ*, **865**, 59
- Lazarian A., Esquivel A., Crutcher R., 2012, *ApJ*, **757**, 154
- Lazarian A., Yuen K. H., Ho K. W., Chen J., Lazarian V., Lu Z., Yang B., Hu Y., 2018, *ApJ*, **865**, 46
- Li P. S., Lopez-Rodriguez E., Ajeddig H., André P., McKee C. F., Rho J., Klein R. I., 2021, *MNRAS*,
- Mac Low M.-M., Klessen R. S., 2004, *Reviews of Modern Physics*, **76**, 125
- Maron J., Goldreich P., 2001, *ApJ*, **554**, 1175
- McKee C. F., Ostriker E. C., 2007, *ARA&A*, **45**, 565
- Montgomery D., Matthaeus W. H., 1995, *ApJ*, **447**, 706
- Montgomery D., Turner L., 1981, *Physics of Fluids*, **24**, 825
- Oppermann N., et al., 2012, *A&A*, **542**, A93
- Planck Collaboration et al., 2015a, *A&A*, **576**, A104
- Planck Collaboration et al., 2015b, *A&A*, **576**, A105
- Planck Collaboration et al., 2016a, *A&A*, **586**, A136
- Planck Collaboration et al., 2016b, *A&A*, **586**, A141
- Planck Collaboration et al., 2016c, *A&A*, **594**, A25
- Planck Collaboration et al., 2020, *A&A*, **641**, A11
- Roche P. F., Lopez-Rodriguez E., Telesco C. M., Schödel R., Packham C., 2018, *MNRAS*, **476**, 235
- Shebalin J. V., Matthaeus W. H., Montgomery D., 1983, *Journal of Plasma Physics*, **29**, 525
- Tahani M., Plume R., Brown J. C., Soler J. D., Kainulainen J., 2019, *A&A*, **632**, A68
- Tahani M., et al., 2022, arXiv e-prints, p. [arXiv:2201.04718](https://arxiv.org/abs/2201.04718)
- Taylor A. R., Stil J. M., Sunstrum C., 2009, *ApJ*, **702**, 1230
- Wang X., Tu C., Marsch E., He J., Wang L., 2016, *ApJ*, **816**, 15
- Wurster J., Li Z.-Y., 2018, *Frontiers in Astronomy and Space Sciences*, **5**, 39
- Xiao L., Fürst E., Reich W., Han J. L., 2008, *A&A*, **482**, 783
- Xu S., Hu Y., 2021, *ApJ*, **910**, 88
- Xu S., Lazarian A., 2020, *ApJ*, **894**, 63
- Xu S., Yan H., 2013, *ApJ*, **779**, 140
- Xu S., Zhang B., 2016, *ApJ*, **824**, 113
- Yan H., Lazarian A., 2002, *Phys. Rev. Lett.*, **89**, 281102
- Yan H., Lazarian A., 2004, *ApJ*, **614**, 757
- Yuen K. H., Lazarian A., 2017a, arXiv e-prints, p. [arXiv:1703.03026](https://arxiv.org/abs/1703.03026)
- Yuen K. H., Lazarian A., 2017b, *ApJ*, **837**, L24
- Zhang H., Gangi M., Leone F., Taylor A., Yan H., 2020, *ApJ*, **902**, L7

This paper has been typeset from a \LaTeX file prepared by the author.